https://doi.org/10.26599/JICV.2026.9210109 Research Article

A modular feed-forward control strategy for vehicle handling enhancement via active wheel alignment

Roberto Aratri [1, ✉], Stefano De Pinto [2,3], Arnau Doria Cerezo [3], Sergio de Bellis [1], Guglielmo Luca Bambino [2], Aldo Sorniotti [4], Francesco Bottiglione [1], Giacomo Mantriota [1]

[1] Department of Mechanics, Mathematics and Management, Polytechnic University of Bari, Bari 70100, Italy

[2] McLaren Automotive Europe, Polígono Industrial L'Albornar, Santa Oliva 43710, Spain

[3] Institut d'Organització i Control de Sistemes Industrials, Universitat Politecnica de Catalunya, Barcelona 08000, Spain

[4] Department of Mechanical and Aerospace Engineering, Polytechnic University of Turin, Turin 10100, Italy

* Corresponding author.
E-mail address: r.aratri@phd.poliba.it

Received: September 1, 2026; Revised: October 11, 2026; Accepted: October 18, 2026

© The Author(s) 2026. This is an open access article under the terms of the Creative Commons Attribution 4.0 International License (CC BY 4.0, http://creativecommons.org/licenses/by/4.0/).

Just Accepted

Abstract

The growing demand for enhanced handling and stability in high-performance vehicles has led to the development of advanced mechatronic systems, including active wheel alignment (AWA) technologies capable of adjusting wheel toe and camber angles. However, the chassis control literature has a gap on the topic of centralized AWA algorithms integrated within vehicle-level control architectures. This paper presents a modular feed-forward AWA control strategy that enhances vehicle cornering performance, while maintaining a natural driving experience and increasing driver confidence, particularly for high-performance vehicles and non-expert drivers. The unique features of the proposed model-following approach are: i) an innovative hierarchical control structure that decouples vehicle-level

control from actuator-level allocation; ii) a novel optimization-based control allocation algorithm adapted from aerospace applications to manage the redundant AWA actuator suite and ensure robustness against actuator failures; and iii) an original lateral tire model with time-varying linearization, enabling the control effectiveness matrix to decouple the camber and lateral slip contributions while retaining tire nonlinearities. Tested on a high-fidelity, experimentally validated supercar model, the controlled vehicle achieves up to 65.8% reduction in sideslip angle and 81.4% faster lateral acceleration response, compared to the passive configuration, along an extreme transient maneuver.

Keywords

Active wheel alignment, Active camber, Rear-wheel-steering, Active systems, Chassis control system performance, Cornering response.

1. Introduction

As the installed power and vehicle mass continue to increase in modern supercars, the demand for advanced mechatronic systems capable of enhancing both handling performance and stability becomes increasingly critical. Torque vectoring, active roll moment distribution, active dampers, and active aerodynamic devices currently represent some of the most advanced and widely researched vehicle dynamics actuation technologies (Dalboni et al., 2024; Mazzilli et al., 2021).

In recent years, the interest of high-performance vehicle manufacturers has been increasingly shifting toward active wheel alignment (AWA) control, e.g., see the recent developments by Sherman (2024) and Doftek (2026). AWA control refers to the active regulation of wheel alignment angles – specifically toe and camber angles – with the aim of enhancing specific aspects of vehicle dynamics. Depending on the system architecture and control strategy, AWA can maximize lateral performance, improve ride comfort, increase yaw stability, or reduce energy consumption by optimizing the tire-road contact conditions. For instance, in the case of Lamborghini, the integration of AWA reportedly results in increased lateral grip and agility, improved transient responsiveness, and superior stability near the limits of handling (Sherman, 2024).

Despite growing industrial interest, examples of AWA algorithms capable of simultaneously controlling camber and toe angles are still relatively rare in the literature. A significant research effort has been carried out by Ruiz (2013), with dedicated electromagnetic actuators actively adjusting the camber and toe angles of the rear wheels of a high-performance vehicle. However, the proposed approach does not implement a true vehicle-level control logic

Just Accepted

that coordinates wheel positioning to directly influence the vehicle dynamics. Instead, the camber and toe variations are applied based on predefined vehicle conditions and cornering phases (e.g., turn entry or exit), without a systematic approach that shapes the cornering response. A different application is presented by Marotta et al. (2022), where camber and toe control is used to compensate for suspension elasto-kinematics and compliance effects. Nevertheless, also this method remains limited to wheel-level alignment control and does not incorporate a higher-level logic directly managing vehicle dynamics. An initial vehicle-level coordination attempt is described by Malvezzi et al. (2022), where AWA is integrated with an active roll moment distribution system, using a proportional control structure based on lateral acceleration, steering wheel angle, and yaw rate measurements. However, purely feedback-based implementations are unsuitable for high-performance vehicles, as they tend to interfere with the driver's input and to degrade the driving experience and natural vehicle behavior (Henning et al., 2016; Kiencke and Nielsen, 2020; Konig et al., 2014).

Most published AWA research focuses on a single actuation method, either active camber (AC), which adjusts only the wheel camber angle, or rear-wheel-steering (RWS), which manipulates only the rear toe angles. Representative RWS studies include Cao et al. (2024) and H. Zhang et al. (2020), where model predictive control (MPC) is employed with sideslip angle and yaw rate targets. In H. Zhang et al. (2020), the driver steering input is incorporated into the MPC cost function to reduce the steering effort. In contrast, Cao et al. (2024) enforces a zero-sideslip reference to maximize stability. Additional RWS approaches are reported in Peters and Stadelmayer (2019) and in Warth et al. (2019), both based on model-following control strategies. Specifically, Warth et al. (2019) improves stability by shaping the steering input to sideslip angle response characteristic, whereas Peters and Stadelmayer (2019) integrates RWS with torque vectoring, by assigning the lateral force generation to RWS and the direct yaw moment generation to torque vectoring. In the RWS control architecture developed by Park et al. (2020), the feed-forward logic is divided into two specialized modules: a steady-state controller that generates the RWS command as a proportional function of the steering wheel input, and a transient controller that refines the RWS action based on lateral acceleration and yaw rate. Regarding AC control, W. Zhang et al. (2021) uses MPC to regulate the lateral position and yaw rate errors in a path tracking application, whereas Ataei et al. (2019) adopts a linear quadratic regulator (LQR) to control yaw rate, lateral speed, and roll angle. Ruiz (2013; 2015; 2016) propose a vehicle-level control strategy that maximizes the longitudinal and lateral forces generated at the tire-road interface by controlling the wheel camber angle, based on the Milliken moment diagram approach.

Just Accepted

In summary, although vehicle-level control frameworks have been developed for individual actuators such as AC and RWS, a systematic methodology for integrating the complete AWA actuator set – comprising front AC (FAC), rear AC (RAC), and RWS – has yet to be established. This paper addresses the identified gap by proposing a novel AWA control strategy aimed at enhancing the lateral acceleration capability of a high-performance sports vehicle, while maintaining sideslip angle within predefined bounds. The approach leverages the full AWA actuator set (FAC, RAC, and RWS), and is designed to fulfill the following objectives:

- Control the vehicle's yaw rate and sideslip angle through a modular control architecture, structured into a high-level (HL) feed-forward controller and a low-level (LL) control allocation module. The HL controller computes global control demands – namely yaw moment and lateral force variations – to be superimposed to the passive vehicle dynamics. The LL controller then translates these demands into actuator-level commands, while accounting for both the tire-road friction limits and actuator constraints.
- Preserve driving engagement and ensure a natural vehicle response. The feed-forward controller avoids any feedback loop on the controlled degrees of freedom for actuator command generation – i.e., no error between measured and reference vehicle states is used to directly modify the actuator inputs. All corrective actions are intentionally delegated to the human driver to prevent the artificial sensations commonly associated with dominant feedback control.
- Ensure compatibility with other actuators, supporting integration within the redundant control architectures typical of high-performance vehicles.
- Guarantee failure-tolerant operation, maintaining control functionality also in the event of failures affecting one or more AWA actuators.

To meet these targets, the following technical and theoretical contributions are introduced:

- A HL control layer that computes the global vehicle control demand independently of the number and type of actuators, ensuring compatibility of the AWA system with future actuator integration. Vehicle-level control actions are computed within a model-following framework, from the mismatch between the current vehicle model and a reference model, whose geometric and design parameters are selected to shape the desired handling characteristics.
- An identification methodology for the nonlinear tire model parameters of the reference and current vehicles within the HL control framework, based on experimental data and known vehicle design parameters. The resulting models are computationally efficient and capture load transfer effects, suspension kinematics and

Just Accepted

compliance, as well as tire and vehicle nonlinearities, without explicitly modeling all underlying physical dynamics.

- A LL control layer that allocates control actions exclusively to the currently active actuators through an optimization-based control allocation scheme employing an active-set algorithm. Adapted from aerospace applications, this approach ensures control effectiveness while meeting tire–road adhesion constraints, actuator rate and saturation limits, and maintains robustness in presence of actuator failures. In addition, a graphical and analytical investigation is presented to assess how the optimization constraints affect the set of vehicle-level control actions that can be effectively generated.
- A simplified and invertible lateral tire model with time-varying linearization, designed for real-time applications while capturing tire nonlinearities. At each time step, the model computes the decoupled contributions of camber and steering angle variations to lateral tire force generation.

The remainder is structured as follows: Section 2 introduces the experimentally validated vehicle model for control system assessment; Section 3 presents the novel lateral tire model integrated within the LL control strategy; Section 4 describes the overall control architecture, including the HL and LL components; Section 5 evaluates the controller performance in several cornering scenarios; finally, the main conclusions are summarized in Section 6.

2. Vehicle modeling

The case study vehicle is a rear mid-engine, rear-wheel-drive supercar featuring a twin-turbocharged V8 engine, paired with a 7-speed plus reverse seamless-shift gearbox and a mechanical open differential. The vehicle is fitted with high-performance road tires in a mixed configuration, i.e., wider tires on the rear axle than on the front, to induce naturally understeering behavior.

2.1. Plant model description

A high-fidelity vehicle model was developed using MSC Adams multi-body dynamics software (Hexagon 2023), which was subsequently imported into the VI-CarRealTime simulation platform (VI_grade GmbH, 2023).

The model represents a four-wheel system with 14 degrees of freedom (DoFs), including six for the chassis and two for each unsprung mass, accounting for suspension displacements and wheel rotations. The steering and suspension system models employ nonlinear kinematic and compliance maps, whereas other components – such as the friction brakes and powertrain differential – are modeled with algebraic equations representing instantaneous input-output dependencies, excluding dynamic states or differential equations.

Just Accepted

The vehicle model incorporates version 5.2 of the Pacejka magic formula (MF 5.2, Pacejka, 2005) tire model, provided by the tire manufacturer, which captures combined wheel forces, moments, and relaxation dynamics.

2.2. Plant model validation

The vehicle model was validated against experimental data collected through standard open-loop characterization maneuvers carried out at the Applus+ IDIADA proving ground (Spain), in accordance with applicable ISO procedures. The steady-state response was characterized using "Method 3 – Constant Speed" from ISO 4138 (2012), which specifies the Slow Ramp Steer (SRS) test protocol. Starting from straight-ahead vehicle operation, the SRS maneuver consists of a linear steering wheel input with a slope of 10 deg/s, covering a total angle of 180 deg. Conversely, the dynamic and frequency response characteristics were assessed following the Continuous Sinusoidal Input (CSI) procedure outlined in ISO 7401 (2011), which is based on a sinusoidal steering application, with an amplitude calibrated to induce a steady-state lateral acceleration target of 4 m/s^2, and a frequency sweep ranging from 0 to 3 Hz. All tests were conducted at a constant vehicle speed of 100 km/h and were repeated across ten independent runs for each maneuver type, to minimize the influence of environmental and test-track condition variability on the measured responses.

Fig. 1 depicts the validation of the vehicle's steady-state behavior through the SRS test, by reporting the steering wheel angle δ_{SW} , sideslip angle β, and roll angle ϕ, as a function of the lateral acceleration a_y. The green scatter points labeled "Experimental data" represent measurements from each individual run, while the black curve, titled "Experimental Data Synthesis," is a polynomial regression fitted to the combined experimental results. The dashed dark red line depicts the vehicle model's response to the same driver inputs as those applied during the tests, enabling a direct comparison between model and experimental data.

Just Accepted

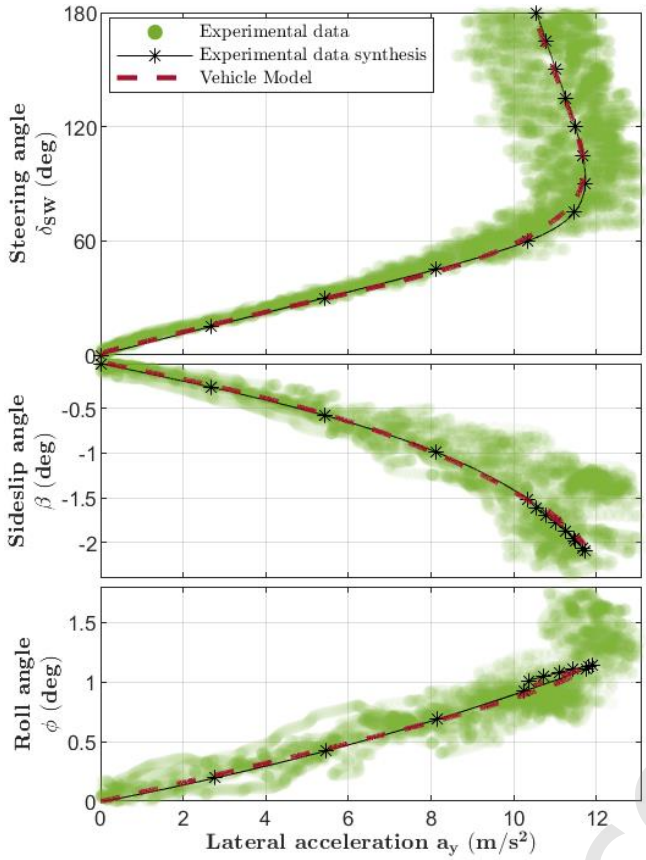


Fig. 1 – Vehicle model validation in steady-state cornering conditions via an SRS test: $\boldsymbol{\delta_{SW}}$, $\boldsymbol{\beta}$, and $\boldsymbol{\phi}$, as a function of $\boldsymbol{a_y}$.

The same methodology is used to validate the frequency response characteristics. In particular, Fig. 2 shows the amplitude and phase of the transfer functions, $G_{\dot{\psi},\delta_{SW}}$ and $G_{a_y,\delta_{SW}}$, relating the yaw rate $\dot{\psi}$ and lateral acceleration to the steering wheel angle input.

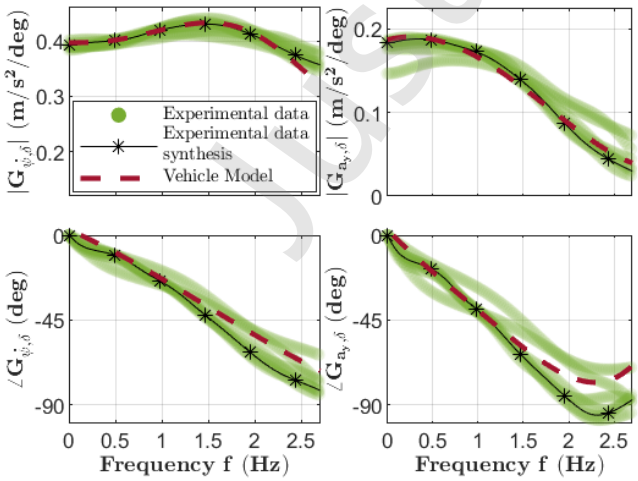


Fig. 2 – Vehicle model validation in transient conditions via a CSI test: frequency response in terms of magnitude and phase of $\boldsymbol{G_{\dot{\psi},\delta_{SW}}}$ and $\boldsymbol{G_{a_y,\delta_{SW}}}$.

Just Accepted

3. The invertible lateral tire model

The AWA control architecture relies on six actuators: four AC actuators – one per wheel – and two RWS actuators. The implementation of the AWA strategy requires a simplified and analytically invertible lateral tire model to determine the variations in camber angle ($\Delta\gamma$) and rear steering angle ($\Delta\delta$) required, at the current tire operating condition, to generate the lateral force variation ΔF_y demanded by the controller to achieve the desired handling response. The corresponding variation in rear slip angle, $\Delta\alpha$, is induced by the RWS steering input $\Delta\delta$. In accordance with the formulations proposed in Ataei et al (2019), the following tire model is adopted:

$$\Delta F_y = K_\alpha \cdot \Delta\alpha + K_\gamma \cdot \Delta\gamma \quad (1)$$

where K_α and K_γ denote the cornering and camber sensitivities, respectively. In the cited works, this formulation is treated as a linear model by assuming constant values of K_α and K_γ, corresponding to the slope of the tire characteristic evaluated at zero slip and camber angles. To improve the physical representativeness of the model while preserving its suitability for real-time control implementation, the present work derives K_α and K_γ from the MF 5.2 tire model and updates them online according to the current operating conditions, resulting in a time-varying linear approximation of the tire behavior. The tire sensitivities are then updated at each subsequent control step according to the current operating conditions.

The proposed offline methodology consists of the following steps:

1. A discrete grid $\mathcal{H}_i$ of slip angles α, camber angles γ, and vertical loads F_z, is defined, where $i = F, R$ denotes front and rear tires, respectively. The grid values adopted for $\mathcal{H}_F$ and $\mathcal{H}_R$ are listed in Table 1.
2. For each point of $\mathcal{H}_i$, the lateral force $F_{y,i}$ is computed using the MF 5.2 model:

$$F_{y,i} = F_{y,i}(\alpha, \gamma, F_z), \text{with } (\alpha, \gamma, F_z) \in \mathcal{H}_i \quad (2)$$

3. The local values of K_α and K_γ are obtained as partial derivatives of $F_{y,i}$ with respect to α and γ, respectively. The lateral force is first averaged over the camber grid $\mathcal{H}_i^\gamma$, and the derivatives are then computed over the discrete ranges of slip angles $\mathcal{H}_i^\alpha$ and camber angles $\mathcal{H}_i^\gamma$: The values of K_α and K_γ are obtained from the variation of $F_{y,i}$ with respect to α and γ, respectively. For the computation of K_α, the lateral force is first averaged over the camber grid $\mathcal{H}_i^\gamma$, and the resulting characteristic is then differentiated with respect to the slip angle. Conversely, K_γ is obtained by evaluating the lateral-force derivative with respect to camber over the discrete camber-angle range and subsequently averaging the resulting values:

Just Accepted

$$K_\alpha = \frac{\partial}{\partial \alpha}\left[\frac{1}{\left|\mathcal{H}_i^\gamma\right|}\sum_{\mathcal{H}_i^\gamma} F_y(\alpha, \gamma, F_z)\right] \quad (3)$$

$$K_\gamma = \frac{1}{\left|\mathcal{H}_i^\gamma\right| - 1}\sum_{\mathcal{H}_i^\gamma} \frac{\partial F_y(\alpha, \gamma, F_z)}{\partial \gamma} \quad (4)$$

where $\left|\mathcal{H}_i^\gamma\right|$ denotes the number of discrete camber angle values in the set $\mathcal{H}_i^\gamma$.

Table 1 – Discrete grids for slip angle $\boldsymbol{\mathcal{H}_i^\alpha}$, camber angle $\boldsymbol{\mathcal{H}_i^\gamma}$, and vertical load $\boldsymbol{\mathcal{H}_i^{Fz}}$, used for front and rear tire analysis.

Grid	Variable	Symbol	Range	Step	Unit
$\mathcal{H}_F$	Slip angle set	$\mathcal{H}_F^\alpha$	[-15;15]	0.5	deg
	Camber angle set	$\mathcal{H}_F^\gamma$	[-4;4]	0.1	deg
	Normal force set	$\mathcal{H}_F^{Fz}$	[0.5;8]	0.5	kN
$\mathcal{H}_R$	Slip angle set	$\mathcal{H}_R^\alpha$	[-15;15]	0.5	deg
	Camber angle set	$\mathcal{H}_R^\gamma$	[-4;4]	0.1	deg
	Normal force set	$\mathcal{H}_R^{Fz}$	[0.5;10]	0.5	kN

Fig. 3 shows the three-dimensional (3D) surface plots of K_α and K_γ as a function of α and F_z, using the rear-right tire as a representative case. As the front tires exhibit similar trends, their results are not reported for brevity. It is worth noting that K_γ is negative for the right-side tires and positive for the left-side ones, according to the camber sign convention of the vehicle model: a positive camber variation produces a negative lateral force on the right tire and a positive one on the left one. K_α shows a strong dependency on both slip angle and vertical load, while K_γ is nearly insensitive to slip angle and follows a predominantly polynomial trend with respect to vertical load. Therefore, the influence of α on K_γ is neglected, and a quadratic fit is used to model its variation with vertical load, as illustrated by the dark red curve in Fig. 3.

A key advantage of this method is its low computational cost and suitability for real-time control implementation. Specifically, the controller can exploit, for both front and rear tires: i) quadratic coefficients (a, b, c) characterizing the load dependence of K_γ; and ii) a look-up table (LUT) describing the variation of K_α as a function of α and F_z. Since the rear slip angles and vertical loads can be reliably estimated through a lightweight approach (detailed in the Appendix), the controller can continuously access accurate tire sensitivity values. This enables the purely feed-forward computation of the camber and rear steering angle adjustments required to generate the desired lateral force.

Just Accepted

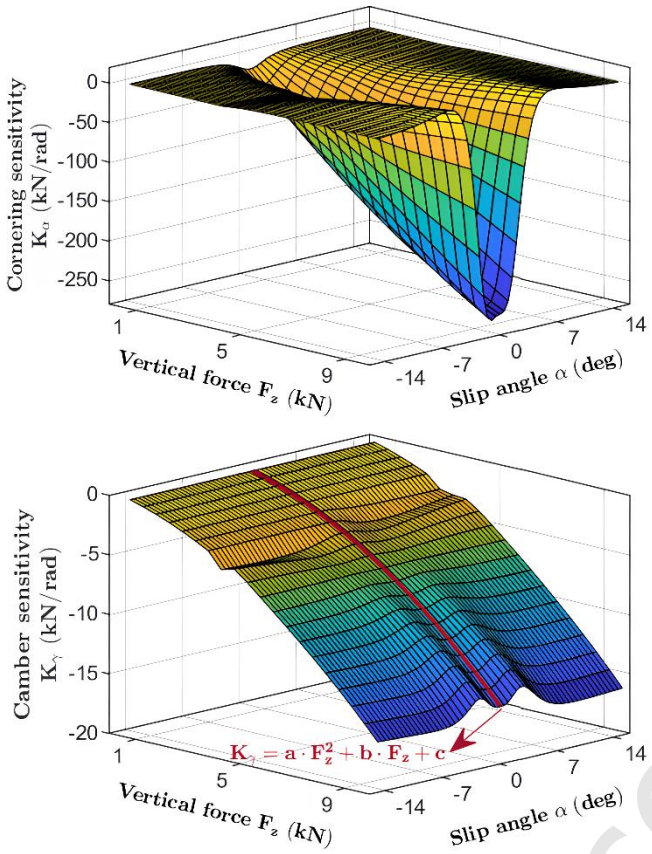


Fig. 3 – 3D surface plots of cornering $\boldsymbol{K_\alpha}$ and camber $\boldsymbol{K_\gamma}$ sensitivities as a function of slip angle $\boldsymbol{\alpha}$ and vertical load $\boldsymbol{F_z}$, for the rear-right wheel.

4. Control framework

This section presents the architecture of the feed-forward controller, which computes the control input vector $\boldsymbol{u}$, including the AC and RWS angle variations, to ensure that the vehicle handling performance matches the target yaw rate and sideslip angle.

The controller is organized into two layers:

- The HL control strategy, which computes the desired control actions, included in the respective vector $\boldsymbol{v^{des}}$, to be applied to the vehicle's center of gravity (CG), based on a model-following control approach.
- The LL control strategy, which distributes the global control actions to the individual actuators through an optimization-based allocation process.

One of the main advantages of this hierarchical architecture is that the HL control strategy remains entirely independent of the specific actuator configuration. This allows the controller to operate seamlessly regardless of the

Just Accepted

number and type of actuator available to deliver the desired effect. Such decoupling enhances both system reliability and flexibility, enabling actuator failures or reconfigurations to be handled without altering the core control logic.

As illustrated in Fig. 4, the controller receives three distinct sets of input signals: i) the driver input vector $\boldsymbol{\sigma_d}$, including clutch, throttle, brake, steering, and gear selection inputs; ii) the state measurement vector $\boldsymbol{y}$ from the vehicle model, consisting of the vehicle velocity V, longitudinal acceleration a_x, lateral acceleration a_y, and yaw rate $\dot{\psi}$; and iii) the estimated state vector $\hat{\boldsymbol{x}}$, containing the non-measurable variables that are required for the operation of the control strategy, namely the longitudinal, lateral and normal wheel loads and rear slip angles. The control framework in Fig. 4 does not currently incorporate actuator models for converting the control commands into voltage and current signals suitable for actual actuator operation. This reflects the preliminary stage of control system development, preceding the specification and detailed design of the actuators. Hence, the strategy presently outputs the computed AC and RWS angle variations directly to the plant model. Despite the absence of explicit actuator models, the control strategy accounts for realistic actuation constraints by incorporating saturation limits, representing the admissible actuator range, and conservative rate limiters, to approximate both computational delays and the finite dynamic response of the actuators. Since actuator dynamics and compliance cannot yet be precisely quantified, the chosen saturation and rate limits are based on literature values and prior studies of actuators with similar characteristics (Malvezzi et al. (2022); Ataei et al. (2019); Ruiz (2013)).

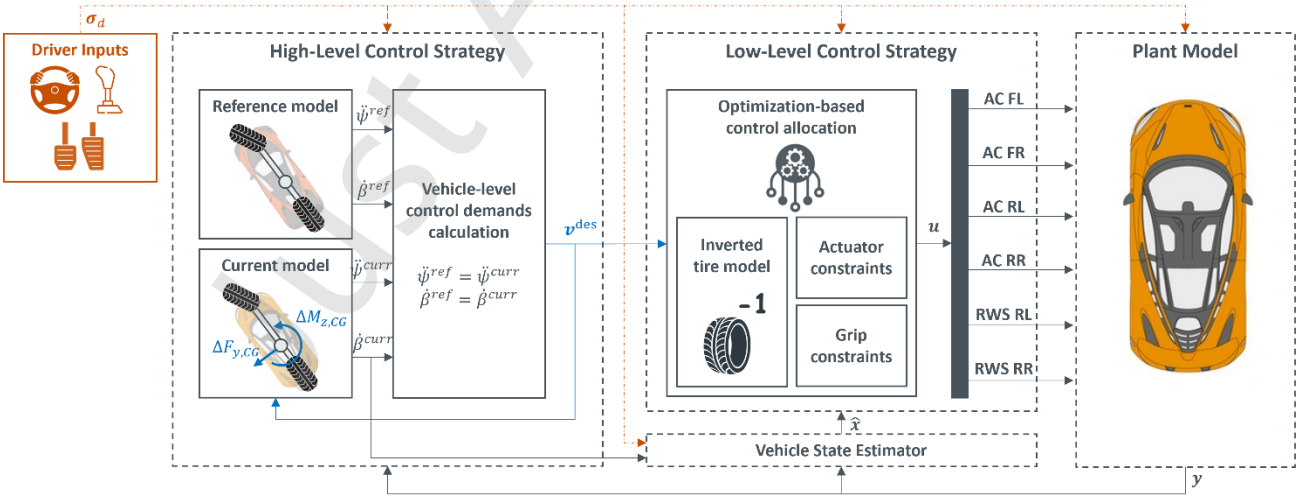


Fig. 4 – Overview of the model-in-the-loop framework with driver model, plant, state estimation, and HL and LL controllers.

4.1. High-level control strategy

The HL control strategy aims to compute the control efforts $\boldsymbol{v^{des}}$ to be applied at the vehicle's CG, i.e. the equivalent lateral force variation $\Delta F_{y,CG}$ and equivalent yaw moment variation $\Delta M_{z,CG}$. The variations refer to the

corresponding passive configuration of the vehicle at the same time instant. The strategy is based on: i) the current vehicle model, which captures the plant's behavior under the effect of $\Delta F_{y,CG}$ and $\Delta M_{z,CG}$ applied to its CG; ii) a reference vehicle model representing the target behavior for the plant in terms of yaw acceleration $\ddot{\psi}$ and sideslip rate $\dot{\beta}$, obtained by modifying vehicle geometric parameters and tire model characteristics using scaling factors; and iii) a model-following layer that calculates $\Delta F_{y,CG}$ and $\Delta M_{z,CG}$ by aligning $\ddot{\psi}$ and $\dot{\beta}$ between the reference and current vehicle models.

Since the controller's performance is highly sensitive to the accuracy of the reference and current vehicle models, which – at the same – must be computationally efficient, two enhanced bicycle-model formulations are employed. The models incorporate the lateral tire grip characteristics through a simplified Pacejka model formulation:

$$\mu_{y,i} = \mu_i \sin\big(C_i \operatorname{atan}\big(B_i\alpha_i - E_i(B_i\alpha_i - \operatorname{atan}(B_i\alpha_i))\big)\big) \quad (5)$$

The tire model parameters B_i, C_i, μ_i, and E_i are identified from two simulated SRS tests, according to a procedure inspired by the method proposed in Aratri et al. (2025) for evaluating the handling stability ratio. This approach relies on knowledge of key vehicle parameters, including the mass m, yaw mass moment of inertia I_{zz}, front and rear semi-wheelbases (l_F, l_R), total wheelbase l, and front and rear aerodynamic downforce coefficients ($C_{df,F}$ and $C_{df,R}$).

The front axle lateral grip characteristic, $\mu_{y,F} = \mu_{y,F}(\alpha_F)$, is identified using data collected during a simulated SRS maneuver performed with standard front tires. The measured signals include the lateral acceleration a_y, yaw acceleration $\ddot{\psi}$, mean steering angle at wheel δ, and sideslip angle β. The identification is carried out through the following equations:

$$\mu_{y,F} = \frac{F_{y,F}}{F_{z,F}} = \frac{m l_R a_y + I_{zz}\ddot{\psi}}{m g l_R + l \cdot C_{df,F} V^2} \quad (6)$$

$$\alpha_{\mathrm{F}} = -\beta - \frac{l_F \dot{\psi}}{V} + \delta \quad (7)$$

Similarly, the rear axle characteristic, $\mu_{y,R} = \mu_{y,R}(\alpha_R)$, is identified from a simulated SRS conducted with better performing (e.g., slick tires, wider tires) front tires, to saturate the rear axle lateral force before the front one. In this case, the characteristic is derived using the following equations:

$$\mu_{y,R} = \frac{F_{y,R}}{F_{z,R}} = \frac{m l_F a_y - I_{zz}\ddot{\psi}}{m g l_F + l \cdot C_{df,R} V^2} \quad (8)$$

$$\alpha_R = -\beta + \frac{l_R \dot{\psi}}{V} \quad (9)$$

Just Accepted

Finally, the parameters B_i, C_i, μ_i, and E_i for the front and rear axles are identified through two separate optimization routines, aimed at fitting the lateral grip characteristics, $\mu_{y,F} = \mu_{y,F}(\alpha_F)$ and $\mu_{y,R} = \mu_{y,R}(\alpha_R)$. The optimizations were carried out using MATLAB's `fmincon` function.

A detailed description of each layer of the HL control strategy is presented in the remainder.

4.1.1. The current vehicle model

The current vehicle model receives as inputs the steering wheel angle δ_{SW} from the driver module, the measured velocity V and longitudinal acceleration a_x, along with the desired control actions $\Delta F_{y,CG}$ and $\Delta M_{z,CG}$. The outputs provided to the model-following layer are the front and rear lateral tire forces $F_{y,F}^{curr}$ and $F_{y,R}^{curr}$, the sideslip angle β^{curr}, and the yaw rate $\dot{\psi}^{curr}$. Here and in the remainder, the apex '$curr$' is used to refer to the variables of the current vehicle model.

The model equations are:

$$\dot{V} - V\beta^{curr}\left[\dot{\beta}^{curr} + \dot{\psi}^{curr}\right] = a_x \tag{10}$$

$$\begin{aligned} F_{y,F}^{curr}\cos(\delta) + F_{y,R}^{curr} + \Delta F_{y,CG} \\ = m\{\dot{V}\beta^{curr} \\ + V\left[\dot{\beta}^{curr} + \dot{\psi}^{curr}\right]\} \end{aligned} \tag{11}$$

$$l_F F_{y,F}^{curr}\cos(\delta) - l_R F_{y,R}^{curr} + \Delta M_{z,CG} = I_{zz}\ddot{\psi}^{curr} \tag{12}$$

The vertical axle loads are computed considering the static weight distribution, aerodynamic downforce, and longitudinal load transfer due to a_x:

$$F_{z,F}^{curr} = \frac{mgl_R}{l} + C_{df,F}V^2 - \frac{ma_x h_{CG}}{l} \tag{13}$$

$$F_{z,R}^{curr} = \frac{mgl_F}{l} + C_{df,R}V^2 + \frac{ma_x h_{CG}}{l} \tag{14}$$

where h_{CG} is the height of the vehicle CG above the ground.

The slip angles α_i^{curr} of each axle evolve according to a first-order dynamic model, with a time constant determined τ_i^{curr}:

$$\tau_F^{curr} \cdot \dot{\alpha}_F^{curr} + \alpha_F^{curr} = \delta - \beta^{curr} - \frac{l_F\dot{\psi}^{curr}}{V} \tag{15}$$

$$\tau_R^{curr} \cdot \dot{\alpha}_R^{curr} + \alpha_R^{curr} = -\beta^{curr} + \frac{l_R\dot{\psi}^{curr}}{V} \tag{16}$$

The time constant τ_i^{curr}, expressed in seconds, is obtained by dividing the corresponding relaxation length $L_{w,i}^{curr}$, expressed in metres, by the vehicle speed V. The relaxation length $L_{w,i}^{curr}$ is evaluated as a function of the current

Just Accepted

vertical load $F_{z,i}^{curr}$ according to the MF 5.2 tire-model formulation [19], using the tire parameters provided by the manufacturer.

Finally, the front and rear lateral forces are computed via the simplified Pacejka tire model in Eq. (5):

$$F_{y,i}^{curr} = F_{z,i}^{curr}\mu_i \sin\big(C_i \operatorname{atan}\big(B_i\alpha_i^{curr} - E_i(B_i\alpha_i^{curr} - \operatorname{atan}(B_i\alpha_i^{curr}))\big)\big) \quad (17)$$

4.1.2. The reference vehicle model

The reference vehicle model receives as inputs only δ_{SW}, V, and a_x. The outputs provided to the model-following layer are the same as those of the current vehicle model: the front and rear lateral forces $F_{y,F}^{ref}$ and $F_{y,R}^{ref}$, the sideslip angle β^{ref}, and the yaw rate $\dot{\psi}^{ref}$, where the apex 'ref' indicates the variables from the reference model.

The dynamic behavior of the reference model is governed by the same set of equations as the current model (from Eq. (10) to Eq. (17)). However, since the reference model represents the target behavior the vehicle should follow, its vehicle parameters and tire model coefficients are adjusted to shape its response in a desirable manner. Specifically, the following scaling factors are introduced:

- The CG height scaling factor k_{CG}, which influences the impact of the longitudinal acceleration on the load transfer.
- The relaxation length scaling factor k_τ, which is applied equally to both axles and adjusts the lateral response dynamics without altering the front-to-rear balance.
- The cornering stiffness scaling factors $k_{B,F}$ and $k_{B,R}$, which influence the linear cornering response, specifically in terms of understeer and sideslip gradients.
- The grip scaling factors $k_{\mu,F}$ and $k_{\mu,R}$, which adjust the tire parameter μ, impacting the cornering stiffness and the maximum grip of each axle. These parameters influence both the linear and nonlinear handling behavior by modifying the axle peak lateral force and, consequently, the maximum lateral acceleration and sideslip angle achievable at a given V.
- The shape scaling factors $k_{E,F}$ and $k_{E,R}$, which alter the front and rear E parameters of the tire model, shaping the vehicle behavior in the post-limit region.

4.1.3. The model following layer

Just Accepted

The model following layer involves the computation of $\Delta F_{y,CG}$ and $\Delta M_{z,CG}$ to ensure that the yaw acceleration and sideslip rate of the current vehicle match those of the reference model, thereby achieving the desired yaw and sideslip dynamics, as detailed in the following equations:

$$\begin{cases} \ddot{\psi}^{curr} = \ddot{\psi}^{ref} \\ \dot{\beta}^{curr} = \dot{\beta}^{ref} \end{cases} \tag{18}$$

By substituting Eqs. (10)-(12) and their counterparts from the reference model into Eq. (18), the following formulations can be obtained:

$$\begin{aligned} \Delta F_{y,CG} = {} & \left[F_{y,F}^{ref} - F_{y,F}^{curr}\right]\cos(\delta) \\ & + \left[F_{y,R}^{ref} - F_{y,R}^{curr}\right] \\ & - ma_x\left[\beta^{ref} - \beta^{curr}\right] \\ & - mV\left\{\dot{\psi}^{ref}\left[1 + \beta^{ref^2}\right]\right. \\ & \left. - \dot{\psi}^{curr}\left[1 + \beta^{curr^2}\right]\right\} \end{aligned} \tag{19}$$

$$\begin{aligned} \Delta M_{z,CG} = {} & l_F\left[F_{y,F}^{ref} - F_{y,F}^{curr}\right]\cos(\delta) \\ & - l_R\left[F_{y,R}^{ref} - F_{y,R}^{curr}\right] \end{aligned} \tag{20}$$

4.2. Low-level control strategy

This section addresses the allocation of $\Delta F_{y,CG}$ and $\Delta M_{z,CG}$ across the control input vector $\boldsymbol{u} = [u_1 \quad \cdots \quad u_6]^T$, which consists of the AC commands for the front-left (FL), front-right (FR), rear-left (RL), and rear-right (RR) wheels, as well as the left and right RWS angles.

Due to the presence of six control inputs and only two control targets, the system is inherently underdetermined, offering four degrees of freedom. To resolve this redundancy and determine a unique solution, the control problem is formulated as a constrained optimization:

$$\min_{\boldsymbol{u}} ||\boldsymbol{Bu} - \boldsymbol{v^{des}}||^2 \quad \text{s.t.} \quad \begin{cases} \boldsymbol{s} \le \boldsymbol{u} \le \boldsymbol{d} \\ \boldsymbol{Cu} \le \boldsymbol{c} \end{cases} \tag{21}$$

where the vectors $\boldsymbol{s}$ and $\boldsymbol{d}$ represent actuator-level bounds; the matrix $\boldsymbol{C}$ and the vector $\boldsymbol{c}$ encode the vehicle-level constraints related to the tire-road interaction at each corner. These constraints will be elaborated upon in the next section. The matrix $\boldsymbol{B}$, referred to as the control effectiveness matrix, maps the actuator impact on $\boldsymbol{v^{des}}$. Leveraging the invertible tire model in Eq. (1), $\boldsymbol{B}$ is defined as:

$$\boldsymbol{B} = \begin{bmatrix} K_{\gamma,1}\cos(\delta_1) & K_{\gamma,1}\cos(\delta_1)\left[l_F + 0.5t_F\tan(\delta_1)\right] \\ K_{\gamma,2}\cos(\delta_2) & K_{\gamma,2}\cos(\delta_2)\left[l_F - 0.5t_F\tan(\delta_2)\right] \\ K_{\gamma,3} & -l_R K_{\gamma,3} \\ K_{\gamma,4} & -l_R K_{\gamma,4} \\ -K_{\alpha,1} & l_R K_{\alpha,1} \\ -K_{\alpha,2} & l_R K_{\alpha,2} \end{bmatrix}^T \tag{22}$$

Just Accepted

where $j = 1, 2, 3, 4$ refers to the FL, FR, RL, and RR corners; δ_1 and δ_2 denote the steering inputs of the FL and FR wheels; and t_F is the front track width. The cornering sensitivity term $K_{\alpha,j}$ is negative according to the sign convention adopted in the vehicle model, where a positive steering input produces a negative slip angle.

4.2.1. Optimization problem constrains

The optimization problem constraints are grouped into three categories:

- Actuator saturation constraints, which limit each control input within a minimum and maximum values defined in the vectors $\boldsymbol{u^{min}}$ and $\boldsymbol{u^{max}}$:

$$\boldsymbol{u^{min}} \leq \boldsymbol{u} \leq \boldsymbol{u^{max}} \quad (23)$$

As specific actuator models are not available, the saturation limits were selected to the best of the authors' knowledge. These limits are intentionally more conservative than those typically reported in the literature (Malvezzi et al., (2022); Ataei et al. (2019); Ruiz (2013)). The selected bounds are defined as:

$$\boldsymbol{u^{min}} = -[\gamma_{sat} \quad \gamma_{sat} \quad \gamma_{sat} \quad \gamma_{sat} \quad \delta_{sat} \quad \delta_{sat}]^T \quad (24)$$
$$\boldsymbol{u^{max}} = -\boldsymbol{u^{min}}$$

where γ_{sat} and δ_{sat} correspond to 4 deg and 0.8 deg, respectively.

- Actuator rate limitation constraints, which restrict the variation of control inputs between consecutive time steps:

$$\boldsymbol{u^{prev}} + dt \cdot r^{min} \leq \boldsymbol{u} \leq \boldsymbol{u^{prev}} + dt \cdot r^{max} \quad (25)$$

where dt = 5 ms is the controller sampling time, and $\boldsymbol{u^{prev}}$ is the control input vector from the previous time step. For both actuator types, the rate limits are conservatively set as r^{min} = -60 deg/s and r^{max} = 60 deg/s, accounting for the actuator dynamics and control loop delays.

- Tire grip constraints at each corner, ensuring that the combined longitudinal and lateral tire forces do not exceed the available friction. For each corner, an elliptical friction limit is imposed:

$$\left[\frac{\hat{F}_{x,j}}{\mu_{x,j}^{max}}\right]^2 + \left[\frac{\hat{F}_{y,j} + \Delta F_{y,j}}{\mu_{y,j}^{max}}\right]^2 \leq \hat{F}_{z,j}^2 \quad (26)$$

where $\Delta F_{y,j}$ is the actuator-induced lateral force, and $\hat{F}_{x,j}$, $\hat{F}_{y,j}$, and $\hat{F}_{z,j}$ are the estimated longitudinal, lateral, and vertical tire forces from the state estimator detailed in the Appendix. Although the longitudinal and lateral tire friction coefficients $\mu_{x,j}^{max}$ and $\mu_{y,j}^{max}$ are assumed constant in this study, in a real-vehicle implementation time-varying values could be obtained via an on-board grip estimation module. By isolating $\Delta F_{y,j}$ in Eq. (26), the following inequality constraints are obtained:

Just Accepted

$$\begin{cases} \Delta F_{y,j} \le \dfrac{\mu_{y,j}^{max}}{\mu_{x,j}^{max}} \sqrt{\left(\mu_{x,j}^{max}\hat{F}_{z,j}\right)^2 - \hat{F}_{x,j}^2} - \hat{F}_{y,j} = g_j^{max} \\ -\Delta F_{y,j} \le \dfrac{\mu_{y,j}^{max}}{\mu_{x,j}^{max}} \sqrt{\left(\mu_{x,j}^{max}\hat{F}_{z,j}\right)^2 - \hat{F}_{x,j}^2} + \hat{F}_{y,j} = g_j^{min} \end{cases} \quad (27)$$

The actuator-level constraints can be expressed in the form of Eq. (21) by defining:

$$\begin{aligned} s_k &= \max\left(u_k^{min}; u_k^{prev} + dt \cdot r^{min}\right) \\ d_k &= \min\left(u_k^{max}; u_k^{prev} + dt \cdot r^{max}\right) \end{aligned} \quad (28)$$

where k ranges from 1 to 6, representing each actuator.

Similarly, the vehicle-level grip constraints can be formulated in the form of Eq. (21) using the tire model introduced in Eq. (1), along with the following definitions:

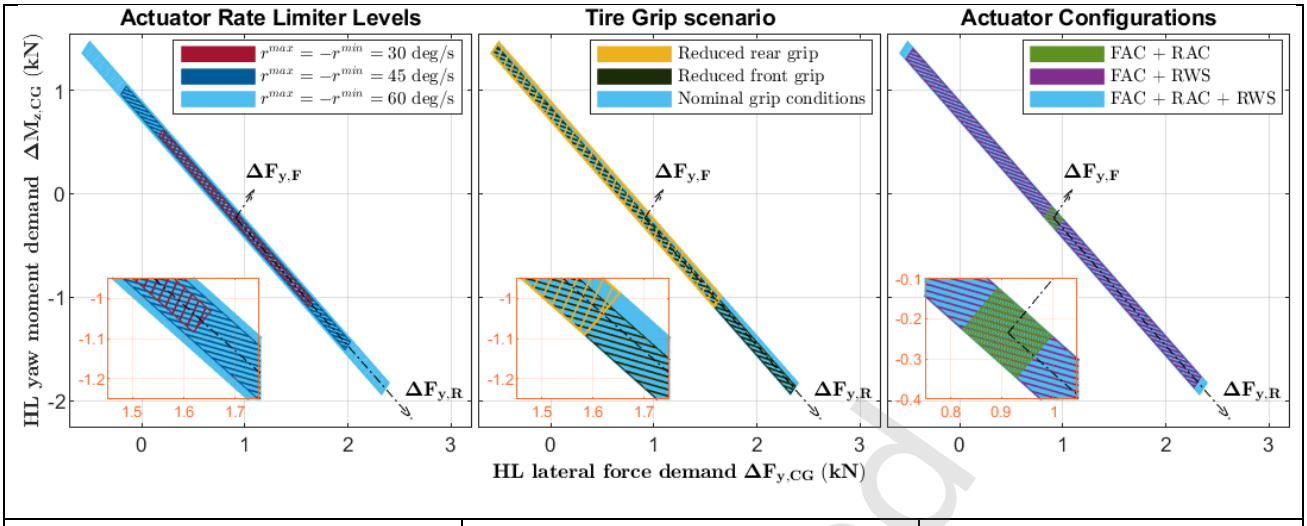
$$\begin{aligned} \boldsymbol{K_\gamma} &= \mathrm{diag}([K_{\gamma,1} \quad K_{\gamma,2} \quad K_{\gamma,3} \quad K_{\gamma,4}]); \\ \boldsymbol{K_\alpha} &= \mathrm{diag}([K_{\alpha,1} \quad K_{\alpha,2}]); \\ \boldsymbol{c} &= [\boldsymbol{g^{max}} \quad \boldsymbol{g^{min}}]^T; \end{aligned} \quad (29)$$

$$\boldsymbol{C} = \begin{bmatrix} \boldsymbol{K_\gamma} & \begin{bmatrix} \boldsymbol{0_2} \\ -\boldsymbol{K_\alpha} \end{bmatrix} \\ -\boldsymbol{K_\gamma} & \begin{bmatrix} \boldsymbol{0_2} \\ \boldsymbol{K_\alpha} \end{bmatrix} \end{bmatrix} \quad (30)$$

where $\boldsymbol{0_2}$ is the zero matrix of order two, and $\mathrm{diag}(\boldsymbol{x})$ denotes a diagonal matrix whose diagonal entries are given by the elements of the vector $\boldsymbol{x}$.

The influence of the individual constraints on the control allocation solution is illustrated in Fig. 5. The figure shows the two-dimensional image Ω of the six-dimensional feasibility region of the optimization problem, mapped onto the $\boldsymbol{v^{des}}$ space. Specifically, Ω represents the image of the constraint set defined in Eq. (21) under the linear transformation induced by matrix $\boldsymbol{B}$, evaluated at an arbitrary time instant. The figure compares how the size of the polygon Ω changes under different operating conditions, assuming that the optimal solution from the previous time step, $\boldsymbol{u^{prev}}$, remains fixed. More specifically, the plots cover: i) variations in actuator rate limits (r^{min}, r^{max}), see Fig. 5(a); ii) different tire-road friction levels (μ_x, μ_y), see Fig. 5(b); and iii) different actuator configurations, see Fig. 5(c).

Just Accepted



(a)	(b)	(c)

Fig. 5 – Representation of the two-dimensional image **Ω** of the six-dimensional feasibility region of the optimization problem under different conditions: **(a)** actuator rate limitations; **(b)** tire grip levels; and **(c)** actuator configurations.

To facilitate the interpretation, each subplot includes a pair of auxiliary axes, $\Delta F_{y,F}$ and $\Delta F_{y,R}$, originating from the point $\boldsymbol{Bu}^{\boldsymbol{prev}}$, which represents the two-dimensional image of the optimization problem solution at the previous time step. These auxiliary axes illustrate how the equivalent HL demand, expressed in terms of $\Delta F_{y,CG}$ and $\Delta M_{z,CG}$, is distributed between the front and rear axles, based on the force and moment balance equations of an equivalent bicycle model:

$$\Delta F_{y,F} = \frac{l_R \cdot \Delta F_{y,CG} + \Delta M_{z,CG}}{l}$$
$$\Delta F_{y,R} = \frac{l_F \cdot \Delta F_{y,CG} - \Delta M_{z,CG}}{l} \quad (31)$$

Under all operating conditions, the image Ω exhibits a rectangular shape, with its sides aligned along the $\Delta F_{y,F}$ and $\Delta F_{y,R}$ directions. This geometric property reflects the decoupled structure of the constraint equations, meaning that actuators operating on different axles are never simultaneously constrained by the same equation.

With reference to Fig. 5(a), the actuator rate limiter constrains the maximum deviation that each actuator control action can exhibit with respect to its value at the previous time step. As a result, decreasing the maximum allowable variation rate leads to a proportional reduction in the lateral force that the controller can generate on both axles, which in turn reduces the area of the convex polygon Ω. Although the rate limit is identical for all actuators, and this constraint equally affects all control actions, the impact of r^{min} and r^{max} appears more pronounced on the rear axle. This effect is due to the higher values of the matrix $\boldsymbol{B}$ entries associated with the rear axle compared to those related to the front one, because of the higher rear cornering sensitivity.

Just Accepted

With reference to Fig. 5(b), a reduction in the tire-road friction coefficient increases the effect of the grip limitation constraints, leading to a reduction in the area of Ω. In particular, a decrease in grip at the front axle reduces the front lateral force that the controller can request, see the green area. Similarly, a reduction in grip at the rear axle limits the controllable rear lateral force, as highlighted by the yellow area. When both axles experience a concurrent grip reduction, the feasible region Ω corresponds to the intersection of the green and yellow areas.

Fig. 5(c) shows the extension of Ω for three actuator configurations: a) with FAC and RAC only; b) with FAC and RWS active; and c) with all three actuators operating simultaneously. Since all three configurations include FAC, the extension of Ω along the $\Delta F_{y,F}$ axis remains unchanged across all conditions, as the controller ability to generate front lateral force is unaffected. On the other hand, given that the cornering sensitivity is more than one order of magnitude higher than the camber one, the system ability to generate rear lateral force is significantly greater when RWS is active. This explains why the purple area extends much further than the green area along the $\Delta F_{y,R}$ axis. Finally, the extension of the light blue area along $\Delta F_{y,R}$ corresponds to the sum of the green and purple areas, as both RAC and RWS are simultaneously active in this configuration.

4.2.2. Optimization problem solution

The control allocation problem is formulated as a constrained least-squares minimization, in which the desired control vector $\boldsymbol{v^{des}}$ is matched as closely as possible by the set of redundant actuators, subject to both actuator-level box constraints and vehicle-level linear constraints, see Eq. (21). The solution is computed using the active-set algorithm that iteratively enforces the relevant inequality constraints, similarly to Harkegard (2025).

The algorithm starts by initializing the control input $\boldsymbol{u}$ based on the previous solution $\boldsymbol{u^{prev}}$. If the initial guess violates any constraint, a corrective projection is applied to restore feasibility. The set of constraints that are exactly saturated at this point defines the initial active set $\mathcal{W}$. At each iteration, the subset of active constraints is treated as a set of equality constraints, and a quadratic Karush-Kuhn-Tucker (KKT) system is solved to compute a search direction. The system includes a regularization term **L** to improve numerical stability for control actions with poor conditioning. The computed direction satisfies the active constraints and seeks to reduce the tracking error with respect to $\boldsymbol{v^{des}}$. A step length α_a is then determined to ensure that the updated control input remains feasible with respect to all inequality constraints. If an inactive constraint becomes saturated along the search direction, it is incorporated into the active set. Conversely, if the projected Lagrange multipliers λ_i associated with the active constraints indicate suboptimality – typically revealed by negative multipliers – the most critical constraint is

Just Accepted

removed from the active set. This iterative process continues until all active constraints are satisfied, the KKT optimality conditions are met, and no further constraints are added or removed. The resulting control input guarantees feasibility with respect to all constraints and minimizes the control allocation error in the least-squares sense.

The complete routine is summarized in Fig. 6. One of the main advantages of employing this type of algorithm to manage actuator redundancy in automotive systems is the high degree of flexibility and failure tolerance. In the event of an actuator failure, or when a change in the actuator hierarchy is desired, the exclusion of a specific actuator can be handled in a straightforward manner, either by removing its corresponding column from the control effectiveness matrix $\boldsymbol{B}$ or by setting its actuation bounds to zero. This eliminates the need for remapping the control architecture or modifying the CPU (central processing unit) logic, making the control allocation scheme scalable and robust to reconfiguration.

Algorithm 1 Active-Set Based Control Allocation

Input: $\mathbf{B} \in \mathbb{R}^{2\times 6}$, $\mathbf{v}^{\text{des}} \in \mathbb{R}^2$, $\mathbf{d}, \mathbf{s}, \mathbf{u}^{prev} \in \mathbb{R}^6$, $\mathbf{c} \in \mathbb{R}^8$, $\mathbf{C} \in \mathbb{R}^{8\times 6}$

Build equivalent constraint set:

$$\mathbf{C}^{\text{eq}} \leftarrow \begin{bmatrix} \mathbf{I}_6 \\ -\mathbf{I}_6 \\ \mathbf{C} \end{bmatrix}, \quad \mathbf{c}^{\text{eq}} \leftarrow \begin{bmatrix} \mathbf{d} \\ -\mathbf{s} \\ \mathbf{c} \end{bmatrix}$$

Initialize: $\mathbf{u}^{(0)} \leftarrow \mathbf{u}^{\text{prev}}$, $\varepsilon > 0$

If $\mathbf{u}^{(0)}$ violates any constraint in $\mathbf{C}_{\text{eq}}\mathbf{u} \le \mathbf{c}_{\text{eq}}$, **then** project onto the feasible set.

Active set: $\mathcal{W} \leftarrow \{n \mid \mathbf{C}_{\text{eq},n}\mathbf{u}^{(0)} = \mathbf{c}_{\text{eq},n} - \varepsilon\}$

for $it = 0, 1, \ldots, it_{\max}$ **do**

  Extract active constraints:

$$\mathbf{C}_{\mathcal{W}} \leftarrow \text{rows of } \mathbf{C}_{\text{eq}} \text{ indexed by } \mathcal{W},$$
$$\mathbf{c}_{\mathcal{W}} \leftarrow \text{corresponding entries of } \mathbf{c}_{\text{eq}}$$

  Build KKT system:

$$\begin{bmatrix} 2\mathbf{B}^\top\mathbf{B} + \mathbf{L} & \mathbf{C}_{\mathcal{W}}^\top \\ \mathbf{C}_{\mathcal{W}} & \mathbf{0} \end{bmatrix} \begin{bmatrix} \Delta\mathbf{u} \\ \boldsymbol{\lambda} \end{bmatrix} = \begin{bmatrix} -2\mathbf{B}^\top(\mathbf{B}\mathbf{u}^{(k)} - \mathbf{v}^{\text{des}}) \\ \mathbf{c}_{\mathcal{W}} - \mathbf{C}_{\mathcal{W}}\mathbf{u}^{(k)} \end{bmatrix}$$

  where $\mathbf{L} \in \mathbb{R}^{6\times 6}$ is the diagonal regularization matrix

  Solve for $\Delta\mathbf{u}$ and $\boldsymbol{\lambda}$

  if $\|\Delta\mathbf{u}\| < \varepsilon$ **then**

    if all $\lambda_n \ge -\varepsilon$ **then**

      return $\mathbf{u}^{(it)}$

    else

      Remove constraint with most negative λ_n from $\mathcal{W}$

    end if

  else

    Compute maximum feasible step size:

$$\alpha_a = \min_{n\notin\mathcal{W},\ \mathbf{C}_{\text{eq},n}\Delta\mathbf{u}>0} \left(\frac{\mathbf{c}_{\text{eq},n} - \mathbf{C}_{\text{eq},n}\mathbf{u}^{(k)}}{\mathbf{C}_{\text{eq},n}\Delta\mathbf{u}} \right)$$

    Update solution: $\mathbf{u}^{(it+1)} = \mathbf{u}^{(it)} + \alpha_a\Delta\mathbf{u}$

    if $\alpha_a < 1$ **then**

      Add blocking constraint to $\mathcal{W}$

    end if

  end if

end for

Return last feasible $\mathbf{u}$

Just Accepted

Fig. 6 – Simplified pseudo-code of the algorithm for constrained optimization in control allocation.

5. Results

This section evaluates the controller performance by employing either the full actuator set associated with the AWA controller or selected actuator subsets among FAC, RAC, and RWS. The performance assessment is carried out along two open-loop maneuvers: i) a chicane-under-acceleration, designed to analyze vehicle behavior during the cornering acceleration phase; and ii) a power-off reaction, in accordance with ISO 9816 (2018), to assess the vehicle response at corner entry.

Both maneuvers are carried out with a target handling behavior corresponding to higher lateral accelerations and reduced dynamic sideslip angle components. The reference response is obtained by assigning the values in Table 2 to the scaling factors of the reference vehicle model introduced in Section 4.1. The rationale behind each parameter selection is outlined below, based on the authors' engineering experience, subjective driving assessments collected during experimental campaigns, and established handling performance evaluation criteria (Aratri et al., 2025):

- The front axle grip is slightly increased ($k_{\mu,F} = 1.03$) to enhance the ability to generate high lateral accelerations and extend the range of linear vehicle cornering behavior, improving predictability.
- The front tire shape factor is slightly reduced ($k_{E,F} = 0.95$) to ensure a smooth transition into the nonlinear cornering response region and prevent snap oversteer.
- The rear axle cornering stiffness and grip are increased ($k_{B,R} = 1.16$, $k_{\mu,R} = 1.03$) to improve vehicle stability and driver confidence, which is particularly suited for high-performance vehicles driven by non-professional users. Additionally, during braking, the CG height is reduced to mitigate the oversteer induced by the longitudinal load transfer.
- Tire relaxation effects are eliminated ($k_{\tau} = 0$) on both axles to achieve more agile and responsive behavior.
- To preserve the linear balance of the passive vehicle and maintain a consistent driving feel regardless of controller operation, the front cornering stiffness scaling factor $k_{B,F}$ is computed as a function of the other parameters, to maintain the understeer gradient of the passive configuration:

$$k_{B,F} = k_{\mu,F}^{-1}\left\{1 + \frac{B_F C_F \mu_F}{B_R C_R \mu_R}\left[\frac{1 - k_{B,R}\cdot k_{\mu,R}}{k_{B,R}\cdot k_{\mu,R}}\right]\right\}^{-1} \quad (32)$$

Since the selected reference behavior requires coordinated control actions on both axles, the controller was tested exclusively with actuator combinations capable of influencing both axles. Specifically, for each maneuver, the

Just Accepted

passive vehicle performance is compared with the one from the following configurations: i) FAC control combined with RAC control; ii) FAC combined with RWS; and iii) simultaneous deployment of FAC, RAC, and RWS.

Fig. 7 illustrates the positioning of the selected reference behavior within the handling feasibility region of each actuator configuration in steady-state conditions. The feasibility region represents the range of achievable understeer and sideslip characteristics – namely δ_{SW} and β as a function of a_y – obtained through the SRS maneuvers described in Section 2, while accounting for both the actuator-level and vehicle-level constraints introduced in Section 4.2.

Table 2 – Scaling factors adopted to define the target handling behavior.

Scaling factor	Value
k_{CG}	$\min(1; \text{sign}(a_x) + 1)$
k_τ	0.00
$k_{B,F}$	1.06
$k_{\mu,F}$	1.03
$k_{E,F}$	0.95
$k_{B,R}$	1.16
$k_{\mu,R}$	1.03

The understeer characteristics show that all actuator configurations similarly increase the maximum achievable lateral acceleration, primarily because of FAC, which increases the lateral force capacity of the front axle. The configurations including RWS further improve the control authority over the understeer gradient by enabling lateral shifts of the rear axle force characteristic. Regarding the sideslip behavior, the widest feasibility region is achieved with the combination of FAC + RAC + RWS, followed by FAC + RWS and FAC + RAC. This trend reflects the greater contribution of RWS to the generation of the rear lateral force compared to RAC, while FAC alone has no influence on rear axle behavior, consistently with Fig. 5(c).

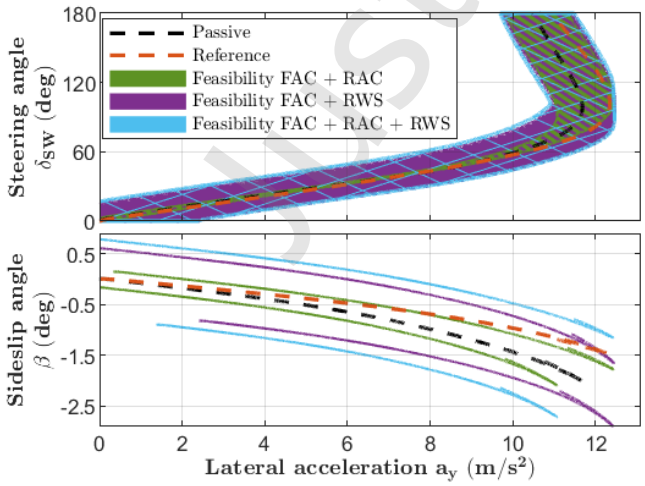


Fig. 7 – Positioning of the selected reference behavior within the feasibility regions of $\boldsymbol{\delta_{SW}}$ and $\boldsymbol{\beta}$ as functions of $\boldsymbol{a_y}$, for: i) FAC + RAC; ii) FAC + RWS; and iii) FAC + RAC + RWS.

Just Accepted

The reference behavior is fully feasible in terms of understeer characteristics across all configurations. However, in terms of sideslip characteristics, the target behavior exceeds the feasibility limits of FAC + RAC beyond a lateral acceleration of ~7 m/s^2, and those of FAC + RWS beyond ~12.2 m/s^2. The reference behavior remains within the feasibility region over the entire lateral acceleration range only for the full actuator set.

The analysis of each open-loop maneuver – reported in the following subsections – is supported by two graphical tools: a) a set of five subplots displaying the driver steering input, and the evolution of V, a_y, $\dot{\psi}$, and β for the passive vehicle, the reference model, and the controlled vehicle under the three actuator configurations, see Fig. 8(a); and b) a set of six subplots, one per actuator, showing the control action profiles, which are marked through red dashed lines in the time intervals characterized by the activation of saturation constraints on the specific actuator, see Fig. 8(b).

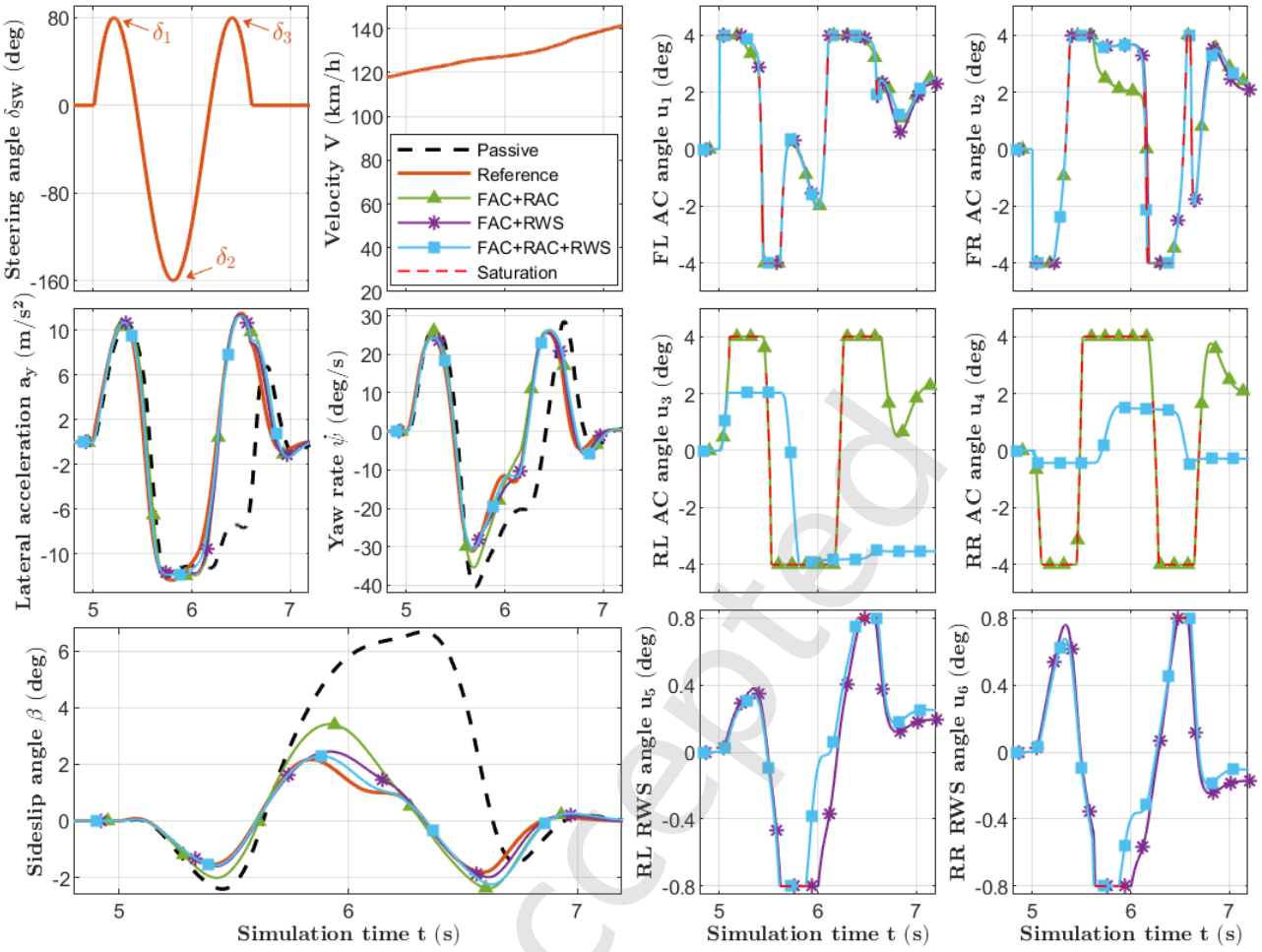
5.1. Chicane-under-acceleration maneuver

The maneuver consists of negotiating a chicane-under-acceleration, to analyze vehicle response in combined cornering and traction conditions. During the test, the steering input ranges from -160 deg to 80 deg, while vehicle speed increases from 120 km/h at the chicane entry to 140 km/h at the exit, see Fig. 8(a). This scenario is very demanding in terms of vehicle stability, especially in the final portion of the maneuver, where values of 28.5 deg/s and 6.7 deg are observed for the third yaw rate peak $\dot{\psi}_3$ and the second sideslip angle peak β_2. A summary of the main key performance indicators (KPIs) is reported in Table 3 for the passive and controlled configurations.

Compared to the passive case, the vehicle equipped with any of the three actuator configurations shows substantial performance improvements. Specifically:

- Vehicle agility is enhanced, with faster dynamics, especially in terms of a_y and $\dot{\psi}$. The time delay $\Delta t_{\delta_3, a_{y,3}}$ between the third steering peak and the corresponding maximum lateral acceleration decreases from 350 ms in the passive vehicle to 65 ms with the full actuator set, marking a 81.4% reduction.
- At equivalent speeds, the lateral acceleration increases significantly, with the third lateral acceleration peak $a_{y,3}$ rising from 6.75 m/s^2 for the passive vehicle to 11.5 m/s^2 with the full actuator set, with a 70.4% increment.
- The overall stability improves, as indicated by the 65.8% and 10.5% reductions of β_2 and $\dot{\psi}_3$ when all actuators are active.

Just Accepted



(a) **(b)**

Fig. 8 – Vehicle response profiles during the chicane-under-acceleration maneuver, performed with the prescribed steering input and speed profiles: **(a)** Comparison of the passive, reference, and controlled configurations; and **(b)** Actuator actions and saturation events.

A performance comparison among the actuator configurations confirms that wider feasibility regions lead to improved accuracy in tracking the desired handling characteristics. The full actuator set (FAC + RAC + RWS) provides the best performance, followed by FAC + RWS and FAC + RAC. This trend is clearly reflected in the β_2 value, with the reference model reaching 2.19 deg, compared to 2.29 deg with FAC + RAC + RWS, 2.44 deg with FAC + RWS, and 3.40 deg with FAC + RAC. As shown in Fig. 8(b), the simultaneous and synergic use of multiple actuators reduces the control effort required from the individual systems. For example, FAC + RAC + RWS improves the reference tracking performance while reducing the RAC control input compared to FAC + RAC, e.g., at $t \approx 5.2$ s, the RL AC and RL AC control actions amount to 2 and -0.2 deg for FAC + RAC + RWS, compared to 4 and -4 deg in the FAC + RAC configuration.

Just Accepted

The FAC + RAC response highlights how actuator prioritization is effectively managed by the LL algorithm. The front-right active camber (FR AC) control action is deliberately limited – below its saturation threshold – around the first steering angle peak at ~5.2 s, to preserve the $\Delta M_{z,CG}$ generation capability. In this phase, increasing FR AC would increase the front lateral force $\Delta F_{y,F}$, which would support the generation of the overall lateral force demand from the HL controller, but would concurrently generate a destabilizing yaw moment. Since RAC is already saturated and cannot provide an additional stabilizing yaw moment, any further $\Delta F_{y,F}$ increase would move $\Delta M_{z,CG}$ away from the HL reference value.

Table 3 also reports KPIs for evaluating the computational efficiency of the iterative active-set-based control allocation algorithm. The KPIs include the average and maximum number (f_{mean} and f_{max}) of solver iterations per time step, as well as the computational efficiency indicator (ϵ_{comp}) of the simulation environment, defined as the ratio between the simulated time window and the real duration of the simulation, measured on a personal computer with an Intel Core i5-7300HQ CPU (4 cores, 2.50 GHz) and 16 GB of RAM, running Windows 10 Home 64-bit. The simulations are performed using a co-simulation setup between MATLAB/Simulink 2023b and VI-CarRealTime 2024. It can be observed that: i) across the feed-forward configurations, with the selected tolerance level the solver requires on average only ~3 iterations per step, with a maximum of 7, thanks to the initialization from the optimal solution at the previous step; ii) while for the active controller the ϵ_{comp} value is roughly half that of the passive configuration, it remains well above unity for all cases; and iii) the FAC + RWS algorithm is the most computationally efficient one, followed by FAC + RAC and the full-actuator configuration, where the last two cases have very similar computational performance.

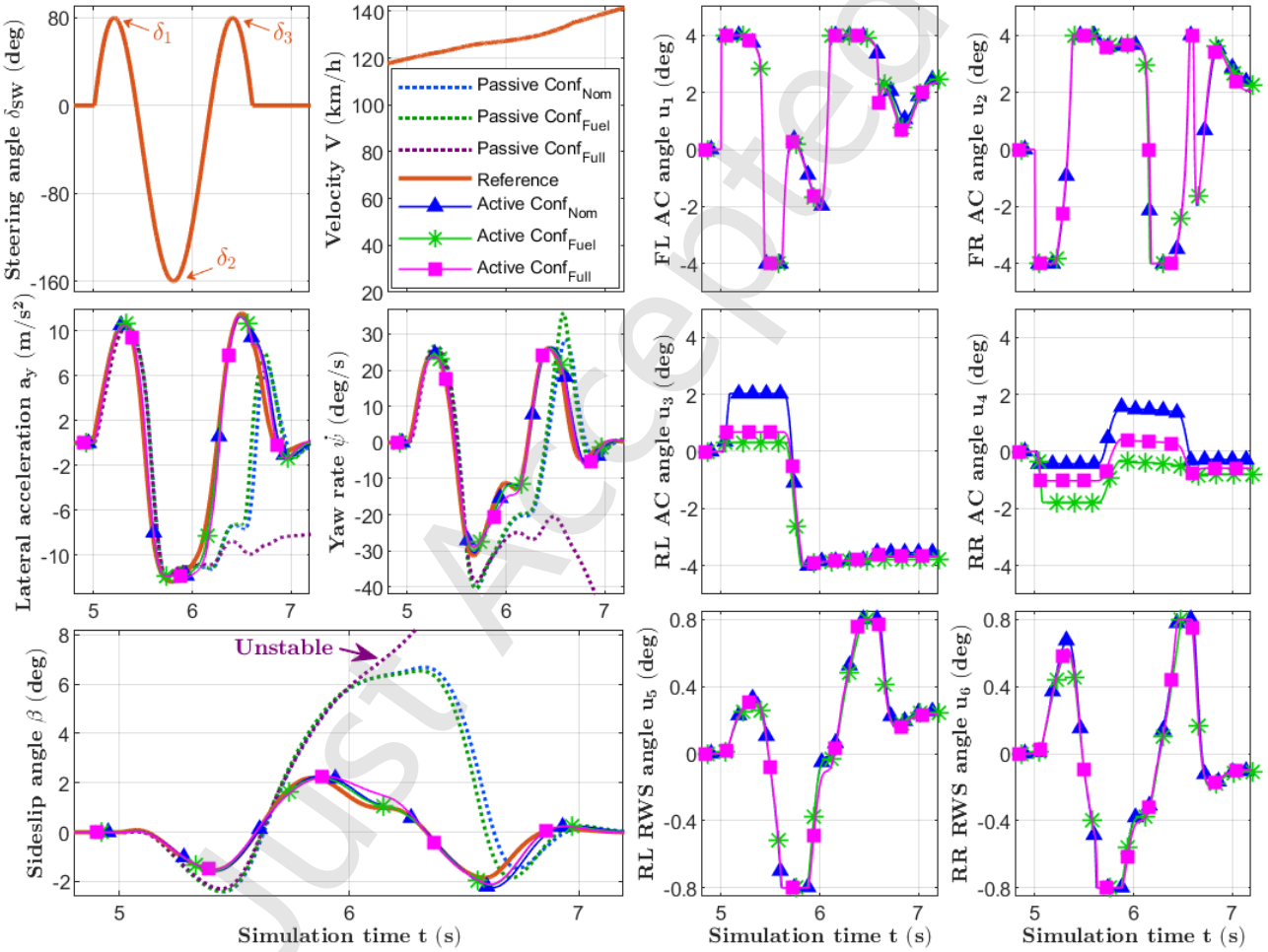
Table 3 – KPIs for the passive vehicle and the controlled configurations during the chicane-under-acceleration and power-off reaction tests

KPI	Unit	Passive	FAC+RAC	FAC+RWS	All
Chicane-under-acceleration maneuver					
β_2	(deg)	6.70	3.40	2.44	2.29
$a_{y,3}$	(m/s^2)	6.75	11.30	11.50	11.50
$\dot{\psi}_3$	(deg/s)	28.50	26.36	26.36	25.50
$\Delta t_{\delta_3,a_{y,3}}$	(ms)	350	100	100	65
it_{mean}	(-)	-	2.95	2.65	3.10
it_{max}	(-)	-	7	7	7
ϵ_{comp}	(s_{sim}/s)	3.18	1.69	1.77	1.66
Power-off reaction test					
β_{min}	(deg)	-5.58	-2.56	-2.25	-1.56
$\%\beta_{OS}$	(%)	174.9	43.8	59.6	10.6

Finally, the chicane-under-acceleration maneuver is employed to evaluate the controller robustness against variations in vehicle running conditions with respect to the design parameters used for control synthesis. Specifically,

Just Accepted

the controller performance is investigated for different load cases. While Fig. 8 considers nominal loading conditions, referred to as "Conf_{nom}" and defined by the presence of a 70 kg driver without additional payloads, Fig. 9 presents the control system performance with two configurations with increased payload and the resulting increase in moments of inertia: i) a fuel-loaded configuration, referred to as "$\text{Conf}_{\text{fuel}}$", corresponding to the vehicle carrying additional 80 kg of fuel with respect to *"$Conf_{nom}$"*; and ii) the fully loaded configuration, "$\text{Conf}_{\text{full}}$", with the vehicle carrying 80 kg of fuel, a 100 kg driver, and a 100 kg passenger, resulting in an increased total mass as well as a forward shift of its distribution.



(a) **(b)**

Fig. 9 – Vehicle response during the chicane-under-acceleration maneuver, performed with the prescribed steering input and speed profiles, for different payload conditions: **(a)** Comparison of the passive, reference, and controlled vehicles; and **(b)** Corresponding actuator actions.

The results indicate that "$\text{Conf}_{\text{fuel}}$" marginally affects the passive vehicle response, with a moderate increase – amounting to 17.6%, 24.1%, and 18.5% – in the third peak values of lateral acceleration, sideslip angle, and yaw rate. In contrast, the fully loaded configuration alters the vehicle mass distribution (from 42% to 45% on the front axle),

Just Accepted

leading to instability in the passive vehicle response. On the contrary, the feed-forward controller ensures stable behavior and satisfactory performance across all considered loading conditions, with substantially overlapped responses for the nominal and "$Conf_{fuel}$" configurations, and only a minor degradation for "$Conf_{full}$". The payload effects are entirely compensated by the RAC actuator, which is the only actuator showing noticeable control action variations. These results highlight the robustness of the proposed feed-forward control strategy also in the absence of an explicit feedback stabilization mechanism.

5.2. Power-off reaction test

The maneuver, defined by ISO 9816 (2018), consists of driving along a constant-curvature path at a fixed speed, using the lowest possible gear to maximize the drivetrain response. Once steady-state cornering is established, the accelerator pedal is abruptly released to induce a rapid longitudinal load transfer. This results in a sudden sideslip angle increase, primarily due to the reduction in rear axle vertical load, thereby exposing the inherent vehicle stability limits. The test is conducted at a steering angle of 100 deg and is repeated for progressively higher steady-state values V_{ss} of the vehicle speed reached prior to the accelerator release, within the range [35-280] km/h, until the test can no longer be completed safely.

Fig. 10 shows the minimum sideslip angle and rate, β_{min} and $\dot{\beta}_{min}$, recorded after the accelerator release, as a function of V_{ss}, for the passive vehicle and the controlled configurations. Interestingly, the trends of β_{min} and $\dot{\beta}_{min}$ are not monotonic across the speed range, since the sideslip dynamics tend to become more critical for higher V_{ss} values for a fixed gear number, but they return to less critical values immediately after the gear number at which the test is executed has to increase because of the engine speed limit. In fact, higher gear numbers correspond to smaller engine braking torque values, and thus to reduced vehicle decelerations and partial mitigation of the induced oversteering effect. The passive vehicle reaches its stability limit for $V_{ss} \approx$ 255 km/h, whereas all controlled configurations remain stable throughout the entire test range. Specifically: i) all actuator combinations markedly reduce the β_{min} and $\dot{\beta}_{min}$ values, compared with the passive case. Even under the most demanding conditions, all controlled configurations maintain β_{min} > -3.5 deg and $\dot{\beta}_{min}$ > -5 deg/s; ii) the different active configurations yield very similar results in terms of β_{min}; and iii) the $\dot{\beta}_{min}$ results indicate that the FAC + RAC + RWS configuration provides the greatest stabilization effect, followed by FAC + RWS and FAC + RAC. In particular, FAC + RWS delivers performance close to FAC + RAC up to 180 km/h, while at higher speeds its behavior approaches the one of the fully actuated configuration.

Just Accepted

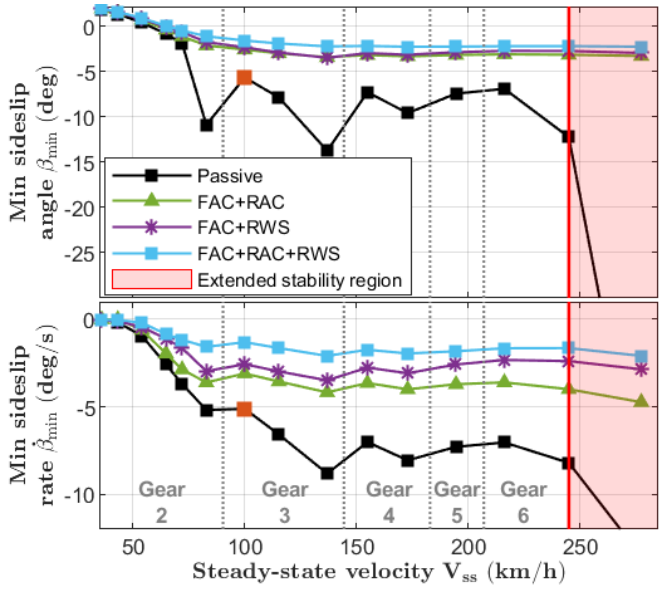
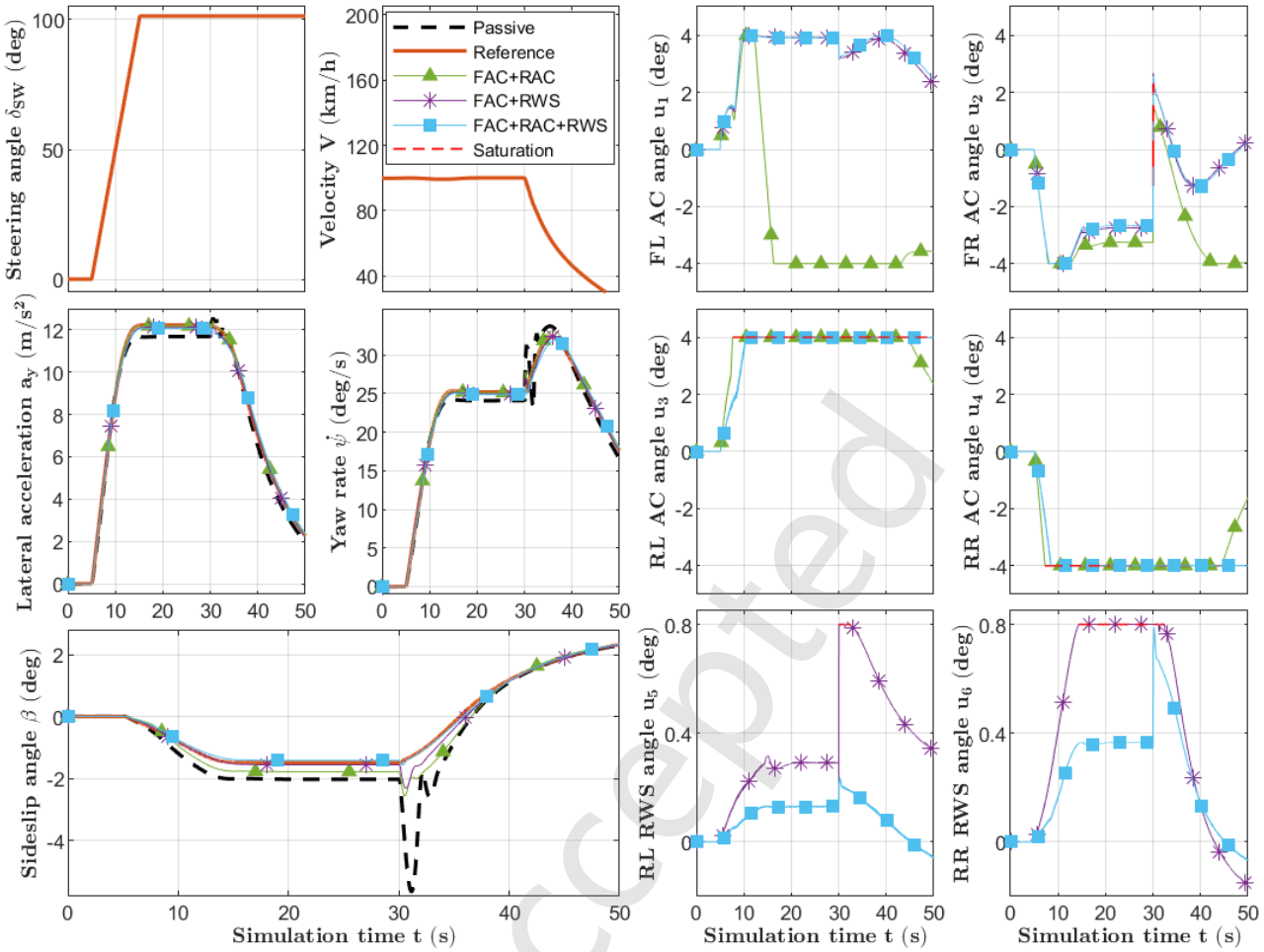


Fig. 10 – Minimum values of the sideslip angle and rate, $\boldsymbol{\beta_{min}}$ and $\boldsymbol{\dot{\beta}_{min}}$, as a function of the steady-state vehicle speed $\boldsymbol{V_{ss}}$, across the power-off reaction tests, for the passive vehicle and the controlled configurations.

Finally, for a detailed assessment of the controller performance benefit, the time profiles of the main variables are reported in Fig. 11 for the power-off reaction test conducted from V_{ss} = 100 km/h in third gear. This test corresponds to the sixth simulation, whose marker is highlighted in orange, within the set of increasing-speed simulations in Fig. 10. Based on the time profiles in Fig. 11(a) and the KPIs in Table 3, upon throttle release, the passive vehicle reaches a β_{min} of -5.58 deg, which – compared with the steady-state value β_{ss} of -2.03 deg – corresponds to a 174.9% sideslip overshoot $\%\beta_{OS}$. Simultaneously, both the yaw rate and lateral acceleration experience large oscillations, with steady-state values of 24 deg/s and 11.7 m/s^2, and peaks of 33.7 deg/s and 12.5 m/s^2. The oversteering trend is increasingly mitigated by the actuator sets, especially in terms of β_{min}, amounting to -2.56 deg, -2.25 deg, and -1.56 deg for FAC + RAC, FAC + RWS, and the full actuator set, which brings a $\%\beta_{OS}$ of only 10.6%. Fig. 11(b) highlights that the limited ability of FAC + RAC and FAC + RWS to track the reference behavior is primarily due to actuator saturation. As already observed in the chicane-under-acceleration, the FAC system reduces its control input during the most critical phase of the maneuver to preserve the target yaw moment contribution $\Delta M_{z,CG}$, at the expense of the generated lateral force $\Delta F_{y,CG}$. In this scenario, the addition of RAC to the FAC + RWS configuration enhances the overall tracking performance while reducing the RWS control effort. For example, shortly after the accelerator release, the RL RWS angle is approximately 0.25 deg with all actuators active, compared with the 0.8 deg in the FAC + RWS configuration, corresponding to the actuator saturation value.

Just Accepted



(a) **(b)**

Fig. 11 – Vehicle response during the power-off reaction maneuver, performed at 100 km/h with a 100 deg steering wheel angle: **(a)** Comparison of the passive, reference, and controlled configurations; and **(b)** Corresponding actuator actions and saturation events.

6. Conclusions

Recent trends in high-performance passenger cars have shifted the focus toward active wheel alignment (AWA) systems, capable of simultaneously adjusting the camber and toe angles in real time to improve cornering performance and enhance driver engagement and confidence. A hierarchical control strategy is required to manage actuator redundancy effectively. To this purpose, a feed-forward AWA control strategy was presented and shown to provide a level of tracking accuracy that supports its potential applicability to real-time vehicle control. For practical vehicle implementation, the proposed feed-forward controller is intended to operate within a closed-loop control framework. Based on the accuracy observed in the investigated scenarios, the feedback contribution is expected to act primarily as a corrective term under nominal operating conditions, preserving natural driving feeling; however, its actual magnitude and its effect on the overall closed-loop behavior require dedicated experimental validation.

Just Accepted

The proposed control architecture is modular and scalable, ensuring compatibility with different vehicle layouts and the additional actuators typically available in high-performance platforms. The high-level control objectives are computed independently of the actuator set, and are subsequently allocated through a constrained optimization problem solved via an active-set algorithm inspired by aerospace applications. After defining a target handling behavior aimed at increasing lateral acceleration and reducing sideslip angle, the control system performance was evaluated for different AWA actuator configurations, along: i) a chicane-under-acceleration, to investigate the response under highly demanding combined dynamics, as well as to verify the robustness for vehicle payload variations not captured by the control and estimation layers; and ii) a power-off reaction test, repeated at progressively increasing speed values, according to ISO 9816 (2018), to assess vehicle stability near the limit of handling.

The main conclusions are:

- The proposed AWA system significantly improves agility and stability, particularly for vehicles equipped with tires characterized by substantial camber sensitivity also in limit handling operation.
- Optimal performance is achieved when all actuators – front active camber, rear active camber, and rear wheel steering – are simultaneously active, providing the widest feasibility control region.
- The controller remains effective under vehicle load variations from the nominal conditions, with significantly reduced performance sensitivity with respect to the passive case.
- The system also performs effectively with partial actuator sets. Specifically, the FAC + RWS configuration achieves results close to the full-actuator case in most scenarios. Conversely, when RWS is excluded, the tracking performance is subject to some degradation even in moderate cornering conditions, although the controller still improves handling and stability relative to the passive configuration.

Future developments will include: a) the integration of actuator dynamics and compliance models into the control framework; b) the enhancement of controller performance under low-grip conditions. Rather than merely limiting the control action according to the available tire-road friction level, a dedicated reference vehicle behavior – together with the re-identification of the tire model parameters – could be implemented for such scenarios; and c) the assessment of controller robustness under actuator failure conditions; and d) the experimental implementation and validation of the algorithm, including evaluation of driver perception and engagement.

Just Accepted

Appendix

This section outlines the estimation method of the wheel loads and rear slip angles, which are not directly measurable with the baseline sensor setup, but are essential for control.

The estimation of the rear slip angles is critical for evaluating the rear tire cornering sensitivities, and is based on the estimated vehicle sideslip angle $\hat{\beta}$, the measured yaw rate $\dot{\psi}$, and the speed V. $\hat{\beta}$ is obtained through an Extended Kalman Filter (EKF), which concurrently estimates the front and rear lateral axle forces $\hat{F}_{y,F}$ and $\hat{F}_{y,R}$, using the measurements of a_y and $\dot{\psi}$, along with the model-based sideslip angle β^{curr} from the HL control layer (Hamann et al. 2014).

The vertical wheel loads $\hat{F}_{z,j}$ are estimated through open-loop formulations accounting for their static distribution, aerodynamic effects, and the longitudinal and lateral load transfers. The longitudinal tire forces $\hat{F}_{x,j}$ are computed through heuristics, from the driver clutch and pedal inputs, engine maps, transmission ratios, rolling resistance coefficients, braking system properties, and ABS status. The lateral tire forces $\hat{F}_{y,j}$ are obtained by distributing $\hat{F}_{y,F}$ and $\hat{F}_{y,R}$ – obtained from the EKF – across the left and right tires proportionally to their vertical loads.

Replication and data sharing

The dataset is available via ETS-Data at https://doi.org/10.26599/ETSD.2025.9190069. It contains simulation results for the Chicane-under-acceleration and power-off reaction tests discussed in Section 5, considering the following vehicle configurations:

- Passive vehicle
- Vehicle equipped with active camber at each wheel
- Vehicle with front active camber and rear wheel steering
- Vehicle with active camber at each wheel combined with rear-wheel steering

The dataset also includes two MATLAB scripts used to load the data and reproduce Fig. 8 and Fig. 11 presented in Section 5.

Just Accepted

Acknowledgements

This work was supported in part by the y the Pedal-Assisted Urban Lightweight Automobile (PAULA) project, Progetti di Rilevante Interesse Nazionale 2022 Piano Nazionale di Ripresa e Resilienza (PRIN 2022 PNRR), under Grant P2022LKJ7Z; and in part by the "Vehicle and Passenger Oriented Holistic Motion Planning for Autonomous Driving" project, PRIN 2022 PNRR, under Grant P2022CL74L.

Declaration of competing interest

The authors declare that they have no known competing financial interests or personal relationships that could have appeared to influence the work reported in this paper.

Citations and References

1. Aratri, R., Guastadisegni, G., De Pinto, S., Doria-Cerezo, A., Sorniotti, A., Bottiglione, F., Mantriota, G., 2025. Feasibility region analysis of active systems: investigating the lateral performance envelope of sports cars. Veh. Syst. Dyn. 63(9), 1676–1697.
2. Aratri, R., De Pinto, S., Guastadisegni, G., Gonzalez, A., Sorniotti, A., Bottiglione, F., Mantriota, G., 2025. On the Development of Vehicle Dynamics Active Systems: The Handling Stability Ratio as a Strategic Indicator for Integrating Multiple Actuators. IEEE Acc. 13, 5634–5647.
3. Ataei, M., Tang, C., Khajepour, A., Jeon, S., 2019. Active camber system for lateral stability improvement of urban vehicles. In: Proceedings of Inst. Mech. Eng., Part D: J. Automob. Eng., 3824–3838.
4. Cao, J., Cao, Y., Leng, B., Liu, M., Wen, H., Xiong, L., et al., 2024. Handling enhancement through active rear-wheel steering with 4WS vehicle reference model. In: Proceedings of the 8th CAA International Conference on Vehicular Control and Intelligence (CVCI), 1–6.
5. Dalboni, M., Mussi, A., Bevilacqua, A., Giorgi, G., Bergamini, E., Sorniotti, A., 2024. On the energy efficiency potential of multi-actuated electric vehicles. *IEEE Trans. Veh. Technol.*, 73, 11150–11167.
6. Doftek, 2026. Doftek. https://www.doftek.com.au [Accessed:31-Aug-2026]
7. Hamann, H., Hedrick, J.K., Rhode, S., Gauterin, F., 2014. Tire force estimation for a passenger vehicle with the Unscented Kalman Filter. In: Proceedings of the IEEE Intelligent Vehicles Symposium (IV), Dearborn, MI, USA, 814–819.

Just Accepted

8. O. Härkegård, 2025. QCAT: Quadratic Programming Control Allocation Toolbox. MATLAB Central File Exchange. https://www.mathworks.com/matlabcentral/fileexchange/4609-qcat. [Accessed:31-Aug-2026].
9. Henning, K.U., Speidel, S., Sawodny, O., 2016. Integrated feed-forward controller for the lateral dynamics of an over-actuated vehicle using optimization-based model inversion. In: Proceedings of the American Control Conference (ACC), Boston, MA, USA, Jul. 6–8.
10. Hexagon MI, MSC Adams multibody dynamics simulation software, version 2023, Troy, MI, USA.
11. International Organization for Standardization (ISO), 2012. *ISO 4138:2012. Passenger cars — Steady-state circular driving behaviour — Open-loop test methods*. Geneva: ISO.
12. International Organization for Standardization (ISO), 2011. *ISO 7401:2011. Road vehicles — Lateral transient response test methods — Open-loop test*. Geneva: ISO.
13. International Organization for Standardization (ISO), 2018. *ISO 9816:2018. Passenger cars — Power-off reaction of a vehicle in a turn — Open-loop test method*. Geneva: ISO.
14. Kiencke, U., Nielsen, L., 2020. *Automotive Control Systems: For Engine, Driveline, and Vehicle*. 2nd edn. Berlin, Germany: Springer, 415–424.
15. König, L., Walter, T., Gutmayer, B., Merlein, D., 2014. Integrated vehicle dynamics control – an optimized approach for linking multiple chassis actuators. In: Proceedings of the 14th Stuttgart International Symposium Automotive and Engine Technology, Stuttgart, Germany, Mar. 18–19.
16. Malvezzi, F., Hess Coelho, T.A., Matarazzo Orsino, R.M., 2022. Feasibility and performance analyses for an active geometry control suspension system for over-actuated vehicles. *J. Braz. Soc. Mech. Sci. Eng.*, 44, 178.
17. Marotta, R., Strano, S., Terzo, M., Tordela, C., Ivanov, V., 2022. Active control of camber and toe angles to improve vehicle ride comfort. *SAE Tech. Pap.*, 2022-01-0920.
18. Mazzilli, V., De Pinto, S., Pascali, L., Contrino, M., Bottiglione, F., Mantriota, G., et al., 2021. Integrated chassis control: Classification, analysis and future trends. *Annu. Rev. Control*, 51, 172–205.
19. Pacejka, H., 2005. *Tire and Vehicle Dynamics*. Burlington, MA, USA: Elsevier.
20. Park, K., Joa, E., Yi, K., Yoon, Y., 2020. Rear-wheel steering control for enhanced steady-state and transient vehicle handling characteristics. *IEEE Access*, 8, 149282–149300.

Just Accepted

21. Peters, Y., Stadelmayer, M., 2019. Control allocation for all-wheel drive sports cars with rear wheel steering. *Automotive and Engine Technology*, 4, 111–123.
22. Ruiz, R., 2013. Active kinematics suspension for a high-performance sports cars. *SAE Tech. Pap*., 2013-01-0684.
23. Ruiz, R., 2013. Method to control toe angle and camber angle in active rear suspensions of cars. U.S. Patent 0 190 980 A1, June, 25.
24. Ruiz, R., 2015. Method of control of an acrive suspension of a car. U.S. Patent 8 930 075 B2, Jan, 6.
25. Ruiz, R., Sabbioni, E., Cheli, F., 2016. Active kinematics suspension integrating Milliken moment method in the control logic. In: Proceedings of the ASME 2016 International Design Engineering Technical Conferences and Computers and Information in Engineering Conference, 1–9.
26. Sherman, J., 2024. Lamborghini's active wheel carrier revealed: Enhancing handling without sacrificing driver feel. *Car and Driver*. https://www.caranddriver.com/news/a46132454/lamborghini-active-wheel-carrier-revealed/ [Accessed: 31-Aug-2026].
27. VI-grade GmbH, 2023. VI-CarRealTime vehicle dynamics simulation software, version 2023, Fulda, Germany.
28. Warth, G., Frey, M., Gauterin, F., 2019. Usage of the cornering stiffness for an adaptive rear wheel steering feedforward control. *IEEE Trans. Veh. Technol.*, 68, 264–275.
29. Zhang, H., Heng, B., Zhao, W., 2020. Path tracking control for active rear steering vehicles considering driver steering characteristics. *IEEE Access*, 8, 98009–98017.
30. Zhang, W., Drugge, L., Nybacka, M., Wang, Z., 2021. Active camber for enhancing path following and yaw stability of over-actuated autonomous electric vehicles. *Vehicle System Dynamics*, 59, 800–821.

Just Accepted

Author biography



R. Aratri received the M.Sc. degree (cum laude) in mechanical engineering from the Politecnico di Bari, Bari, Italy, in 2023, where he is currently pursuing the Ph.D. degree. His research interests include stability and handling analysis of high-performance vehicles with redundant mechatronic systems.



S. De Pinto received the M.Sc. degree in mechanical engineering and the Ph.D. degree in mechanical and automotive engineering from the Politecnico di Bari, Bari, Italy, in 2013 and 2015, respectively. He is currently a Principal Vehicle Dynamics Engineer specialized in active/semi active systems development with McLaren Automotive and an Associate Professor with UPC Barcelona. His main research interests include hybrid electric vehicles, electric vehicles, and vehicle dynamics, with a focus integrated chassis control to improve handling performance and stability.



S. de Bellis received the M.Sc. degree (cum laude) in mechanical engineering from the Politecnico di Bari, Bari, Italy, in 2018, where he is currently pursuing the Ph.D. degree. His research interests include the development of model-based state observers for estimating vehicle variables that cannot be measured directly on board.



G. L. Bambino received the M.Sc degree in mechanical engineering from the Polytechnic University of Turin, Turin, Italy in 2018. He has been working at McLaren Automotive for over six years, where he is currently the Subject Matter Expert for Active Aerodynamics Systems within the High-Level-Control-Strategies team. His main research interests include vehicle dynamics and mechatronics systems, with focus on Active Aerodynamics.



A. D. Cerezo received the M.Sc degree in electromechanical engineering from the Universitat Politècnica de Catalunya, Barcelona, in 2001, a D.E.A. degree in industrial automation from the Institut National des Sciences Appliquées de Lyon, Villeurbanne, France, in 2001, and the PhD degree in advanced automation and robotics from UPC in 2006. He is currently an associate professor at the Department of Electrical Engineering, UPC. He carries on his research activities at the Institute of Industrial and Control Engineering, UPC. His research interests include modeling and control of electrical systems and automotive applications.



A. Sorniotti received the M.Sc. degree in mechanical engineering and the Ph.D. degree in applied mechanics from the Politecnico di Torino, Turin, Italy, in 2001 and 2005, respectively. He is currently a Full Professor in applied mechanics with the Politecnico di Torino, after being a professor in advanced vehicle engineering with the University of Surrey, Guildford, U.K., where

Just Accepted

he led the Centre for Automotive Engineering. His research interest includes vehicle dynamics control of electric and automated vehicles.



F. Bottiglione received the M.Sc. degree (cum laude) in mechanical engineering and the Ph.D. degree in mechanical design and biomechanics from the Polytechnic University of Bari, in 2004 and 2008, respectively. He is currently a Full Professor in applied mechanics with the Department of Mechanics, Mathematics and Management, Polytechnic University of Bari. He is also the Coordinator of the B.Sc. in Aerospace Systems Engineering and of the Laboratory of Tribology, TriboLab, Polytechnic University of Bari. His research interests include the studies of vehicle dynamics, tribology, applied nonlinear dynamics, mechanical transmissions, material science.



G. Mantriota received the Graduate degree (cum laude) in mechanical engineering from the Università di Bari, in 1987, and the Ph.D., M.Sc., and Graduate degrees in mechanical engineering from the Politecnico di Bari, in 1993, 2012, and 2021, respectively. He has been a Full Professor in mechanics applied to machines with the Politecnico di Bari, since 2002. He was the President of the Industrial Engineering Degree (2006–2012). His research interests include hybrid and electric vehicles, vehicle stability control, continuously variable transmissions, articulated vehicle, traction controllers, kinetic energy recovery systems, fuel economy, toroidal traction drives, power split transmissions, hand prosthetic mechanisms, and tracked robot.

Just Accepted